# Higher-Order Topology of the Axion Insulator $EuIn_2As_2$

Yuanfeng Xu,[1,2,3] Zhida Song,[1,2,4] Zhijun Wang,[1,2] Hongming Weng,[1,2,5,6,*] and Xi Dai[7,†]
[1]Beijing National Laboratory for Condensed Matter Physics, and Institute of Physics, Chinese Academy of Sciences, Beijing 100190, China
[2]University of Chinese Academy of Sciences, Beijing 100049, China
[3]Max Planck Institute of Microstructure Physics, Halle 06120, Germany
[4]Department of Physics, Princeton University, Princeton, New Jersey 08544, USA
[5]CAS Center for Excellence in Topological Quantum Computation, University of Chinese Academy of Sciences, Beijing 100190, China
[6]Songshan Lake Materials Laboratory, Dongguan, Guangdong 523808, China
[7]Department of Physics, Hong Kong University of Science and Technology, Clear Water Bay, Kowloon 999077, Hong Kong

(Received 1 April 2019; published 25 June 2019)

Based on first-principles calculations and symmetry analysis, we propose that $EuIn_2As_2$ is a long-awaited axion insulator with antiferromagnetic (AFM) long-range order. Characterized by the parity-based invariant $\mathbb{Z}_4 = 2$, the topological magnetoelectric effect is quantized with $\theta = \pi$ in the bulk, with a band gap as large as 0.1 eV. When the staggered magnetic moments of the AFM phase are along the $a$ or $b$ axis, it is also a topological crystalline insulator phase with gapless surface states emerging on (100), (010), and (001) surfaces. When the magnetic moments are along the $c$ axis, both the (100) and (001) surfaces are gapped, and the material can also be viewed as a high-order topological insulator with one-dimensional chiral states existing on the hinges between those gapped surfaces. We have calculated both the topological surface states and the hinge state in different phases of the system, respectively, which can be detected by angle-resolved photoemission spectroscopy or STM experiments.

DOI: 10.1103/PhysRevLett.122.256402

*Introduction.*—The concept of an axion field is introduced to solve the strong charge-parity ($CP$) problem in quantum chromodynamics [1], while in condensed matter physics, the axion field appears in the field theory description of the topological magnetoelectric (TME) effect [2,3], with an effective action in the form

$$S_\theta = \frac{\theta e^2}{4\pi^2} \int dt d^3\boldsymbol{x} \boldsymbol{E} \cdot \boldsymbol{B}, \tag{1}$$

where $\boldsymbol{E}$ and $\boldsymbol{B}$ are electromagnetic fields and the coefficient $\theta$ is the axion angle with a period of $2\pi$. This term will modify Maxwell's equation in classical electrodynamics and lead to the TME effect [2]. Since the magnetoelectric coupling term $\boldsymbol{E} \cdot \boldsymbol{B}$ will change sign under time reversal symmetry $\mathcal{T}$ or inversion symmetry $\mathcal{I}$, the only allowed value of $\theta$ has to be quantized to 0 or $\pi$ in the systems preserving either $\mathcal{T}$ or $\mathcal{I}$. For three-dimensional (3D) insulators with $\mathcal{T}$ symmetry, the quantized $\theta$ term is related to the $\mathbb{Z}_2$ invariant directly. For the centrosymmetric insulators (breaking $\mathcal{T}$ symmetry), it can be reduced to a parity-based invariant, $\mathbb{Z}_4 = 0, 2$ (note that $\mathbb{Z}_4 = 1, 3$ corresponds to a semimetal with Weyl nodes), which is defined as [4–6]

$$\mathbb{Z}_4 = \sum_{\alpha=1}^{8} \sum_{n=1}^{n_{\mathrm{occ}}} \frac{1 + \xi_n(\Lambda_\alpha)}{2} \mod 4, \tag{2}$$

where $\Lambda_\alpha$ are the eight $\mathcal{I}$-invariant momenta, $n$ is the band index, $n_{\mathrm{occ}}$ is the total number of valence electrons, and $\xi_n(\Lambda_\alpha)$ is the parity eigenvalue $(+1/-1)$ of the $n$th band at $\Lambda_\alpha$. A centrosymmetric insulator with $\mathbb{Z}_4 = 2$ can have a quantized TME effect ($\theta = \pi$), so it is also called an axion insulator (AI). The surfaces of the AI can have a half quantum Hall effect if they are gapped [7]. Very recently, axion insulators have also been proposed to host one-dimensional (1D) chiral states on the hinges and can at the same time be viewed as the newly proposed higher-order topological insulator (HOTI) [8–18].

Although in the literature there are already a number of material proposals for the axion insulator phase including the heterostructure constructed by quantum anomalous Hall insulators [19,20], the magnetically doped 3D TIs [15,21], the axion insulator phase induced by a Coulomb interaction in magnetic osmium compounds [22], and the layered antiferromagnetic (AFM) TI with a type-IV magnetic space group (MSG) [7,23–26], a satisfactory stoichiometric material system with an accessible single crystal is still absent, which greatly impeded the experimental studies on both the AI and the topological magnetoelectric effect.

In the present Letter, we predict that $EuIn_2As_2$ is an AFM axion insulator (breaking $\mathcal{T}$ symmetry, but preserving $\mathcal{I}$ symmetry), no matter which direction the magnetic order is pointing to. Its nontrivial topology can be characterized by the parity-based invariant, $\mathbb{Z}_4 = 2$. The

 

quantized bulk TME effect can be expected in the material with a bulk energy gap of ~0.1 eV. As there are no experimental data to determine the direction of the magnetism (which *does* effect the surface states), we have investigated two AFM phases (i.e., $afmb$ and $afmc$ phases) in the first-principles calculations. The results show that the energy difference of the two phases is less than 1.0 meV. The $afmb$ phase of $EuIn_2As_2$ is described by a type-I MSG, $Cmcm$. Our calculations show it is also a topological crystalline insulator (TCI), characterized by *nonzero* mirror Chern numbers (MCNs) defined on the $k_y = 0$ and $k_z = 0$ planes. As a result, those surfaces perpendicular to one of the mirror planes are gapless. However, the $afmc$ phase belongs to a type-III MSG, $P6_{3'}/m'm'c$, and no symmetry-protected gapless surface state is found for both (100) and (001) surfaces. As a consequence,the $afmc$ phase is a HOTI, and a chiral mode can emerge on the hinge between two of those gapped surfaces, which has also been obtained in our detailed calculations. As $EuIn_2As_2$ is easy to grow and the magnetism is intrinsic and confirmed already by experiments, it is an ideal platform to study the physical properties of the axion insulators and HOTI experimentally.

*Crystal structure and methodology.*—$EuIn_2As_2$ is an antiferromagnetic Zintl compound with the Néel temperature $T_N = 16$ K [27,28]. The magnetism measurements on single-crystal samples show that the moments on $Eu^{2+}$ cations are about $7.0\mu_B$, indicating the high-spin configuration of $4f^7$ on the $Eu^{2+}$ ions. The intralayer exchange coupling among $Eu^{2+}$ ions is ferromagnetic, while the interlayer coupling is antiferromagnetic, leading to $A$-type antiferromagnetic long-range order in the material. The direction of spin polarization detected by the experiments can be along the crystallographic $a$ or $b$ axis [$afmb$ phase as shown in Fig. 1(a)] or $c$ axis [$afmc$ phase as shown in Fig. 1(b)] with a small energy difference between them. The crystal structure of $EuIn_2As_2$ adopts a hexagonal lattice with the space group of $P6_3/mmc$ (No. 194), as shown in Figs. 1(a) and 1(b). It can be generated by the following symmetry operators: $\mathcal{I}$, $C_{3z}$, $C_{2y}$, and $\{C_{2x/z}|00(c/2)\}$, where $[00(c/2)]$ is a half of the lattice translation along the $c$ direction. The experimental lattice constants were adopted throughout the following calculations with $a = b = 4.2055$ Å and $c = 17.887$ Å. The Eu atom is located at the Wyckoff position $2a$ (0, 0, 0). Both In and As are at the $4f$ Wyckoff position with the coordinates of $(2/3, 1/3, 0.17155)$ and $(1/3, 2/3, 0.60706)$, respectively. We have performed the first-principle calculations using the Vienna *ab initio* simulation package (VASP) [29,30], and the generalized gradient approximation (GGA) [31] with the Perdew-Burke-Ernzerhof [32,33] type exchange-correlation potential was adopted. The Brillouin zone (BZ) sampling was performed by using $k$ grids with an $11 \times 11 \times 3$ mesh in self-consistent calculations. As the on-site Coulomb interactions among electrons on Eu-$4f$ orbitals are very strong, we have taken $U_{4f} = 5.0$ eV as a parameter in the GGA + $U$ calculations [34] to locate the occupied $4f$ orbitals at the energy determined by experiments. To calculate the topological surface states and hinge states of antiferromagnetic $EuIn_2As_2$, we have generated the maximally localized WANNIER functions for $5s$ orbitals on In and $4p$ orbitals on As using the WANNIER90 package [35].

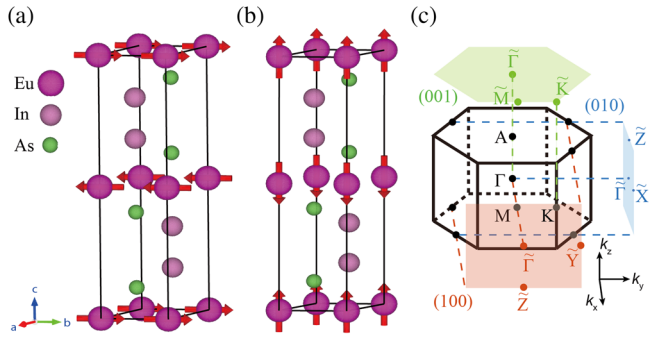


FIG. 1. The crystal and magnetic structure of $EuIn_2As_2$. (a) and (b) are the $afmb$ and $afmc$ phases, respectively. The crystal axes $b$ and $c$ are along the $y$ and $z$ directions in the Cartesian coordinate system, respectively. (c) The bulk BZ and the surface BZ projected onto (100), (010), and (001) surfaces. Here (100) [(010) or (001)] refers to the surface normal vector in terms of the Cartesian coordinate.

*Nodal-line semimetal without SOC.*—We have first calculated the band structure of $EuIn_2As_2$ with an antiferromagnetic phase in the absence of spin-orbit coupling (SOC). We find that without SOC the material will become a nodal-line semimetal when the $A$-type AFM order is fully developed. The AFM-type magnetic order reduces the point group symmetry to $D_{3d}$, generated by $\mathcal{I}$, $C_{3z}$, and $C_{2y}$. The analysis of orbital character shows that the bands near Fermi energy are dominated by $5s$ orbitals of In and $4p$ orbitals of As. Because of the correlation effect, the fully spin-polarized $4f$ orbitals of each Eu are pushed down to 1.5–2.0 eV below the Fermi level, which is quite consistent with the position suggested by experimental measurements [36,37]. The band dispersion along the high-symmetry directions in Fig. 1(c) is shown in Fig. 2(a), which shows that there is a band crossing feature near the Γ point on the Fermi energy. Detailed calculations and further symmetry analysis show that it is actually an anticrossing along the Γ$M$ direction, while the crossing along Γ$K$ is protected by $C_{2y}$ symmetry, as shown in the right panel in Fig. 2(a). Namely, two crossing bands belong to different $C_{2y}$ eigenvalues $\pm 1$ along the Γ$K$ line. Considering the possible underestimation of the band gap by GGA, the band inversion is further confirmed by the calculations using the modified Becke-Johnson potential, where the band inversion is reduced to be around 0.06 eV [38] (see detail in Supplemental Material [39]).

The $\mathbb{Z}_4$ invariant ($n_{\mathrm{occ}} = 146/2$ for each spin channel) is computed to be 1 for the spin-up channel, which implies

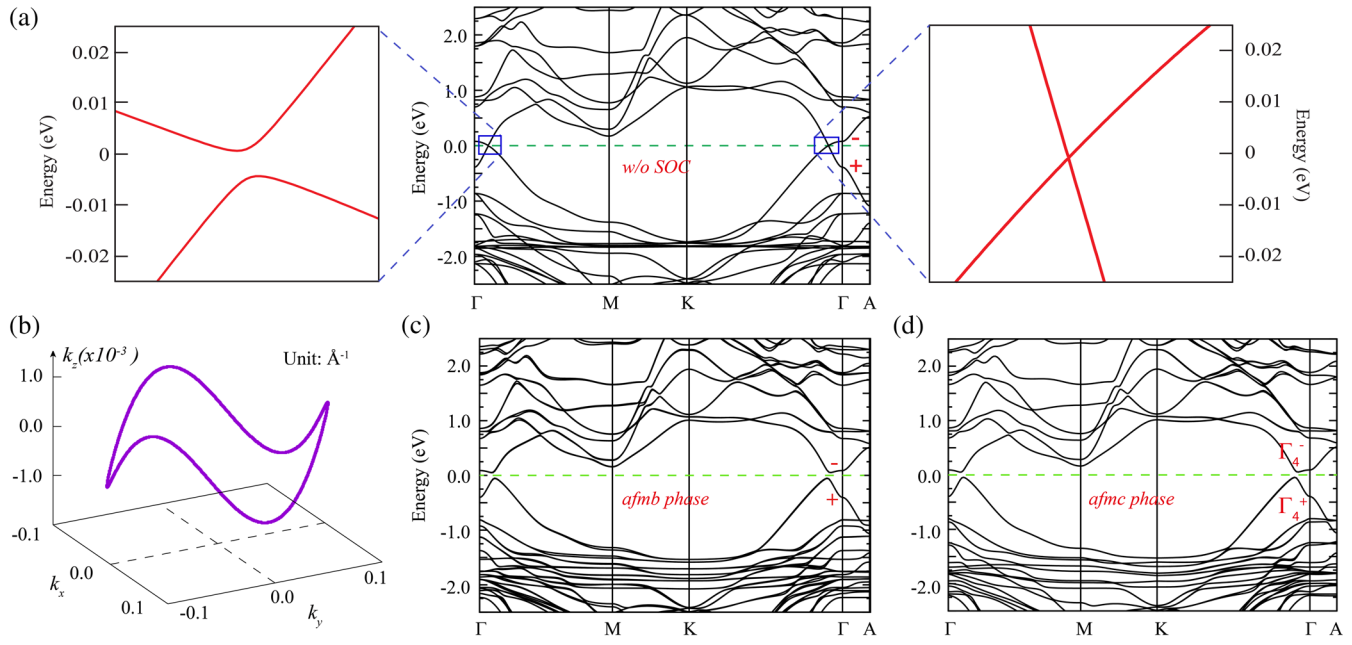


FIG. 2. Electronic band structures along the high-symmetry path in BZ obtained by GGA + $U$ calculations with $U_{4f} = 5.0$ eV. (a) AFM band structure without SOC. The left panel shows the band crossing along $\Gamma M$ is fully gapped, while the right panel shows a nodal point along the $\Gamma K$ path. The parities of the inverted bands have been signed. (b) Symmetry -protected nodal line near the Γ point for the spin-up channel. It is shaped by the point group $D_{3d}$ on Γ. (c) and (d) are the band structures with SOC for $afmb$ and $afmc$ phases, respectively. The minimal energy gap of them is about 0.1 eV.

that there are either nodal lines or odd pairs of Weyl nodes depending on the symmetry. In the collinear magnetic calculations without SOC, the Hamiltonian for each spin channel is still real. There is a symmetry ($C$) of complex conjugation, $C = \mathcal{K}$, which is the same as the time reversal symmetry for spinless systems. Thus, the combined antiunitary symmetry of $C$ and $\mathcal{I}$ satisfies $(C\mathcal{I})^2 = 1$, which forbids one of the three Pauli matrices in a two-band effective model at *any* $k$ point. Therefore, the nodal line is guaranteed by $\mathbb{Z}_4 = 1$. In fact, the crossing point on $\Gamma K$ is part of the nodal line, as shown in Fig. 2(b). The nodal line for the spin-down channel is obtained by a mirror reflection with respect to the $k_z = 0$ plane, because the two spin channels are related to each other by the combined symmetry $\mathcal{T}\{C_{2z}|00(c/2)\}$.

*Axion insulator with SOC.*—As suggested by the previous experiments [27,28], two metastable AFM phases, with the magnetic moment $m||b$ axis ($afmb$ phase) and $m||c$ axis ($afmc$ phase), respectively, have been investigated in our calculations including SOC. These two states are nearly degenerate from our calculations with the energy difference being less than 1 meV. As the bands of $4f$ orbitals are localized far away from the Fermi level, the low-energy band structures of the two AFM phases are very similar. We note that SOC has two main effects: (i) It opens a band gap, which is about 0.1 eV as shown in Figs. 2(c) and 2(d); (ii) it changes the symmetry of the AFM phases, which does effect the behavior of the surface states.

Because of the presence of $\mathcal{I}$ symmetry, one can compute the $\mathbb{Z}_4$ invariant, which is defined on the parity eigenvalues at the eight $\mathcal{I}$-invariant points $\Lambda_\alpha(\alpha = 1, 2, \ldots, 8)$. The number of odd and even bands are listed in Table I. The obtained invariant $\mathbb{Z}_4 = 2$ suggests that $EuIn_2As_2$ is an axion insulator exhibiting a quantized TME effect ($\theta = \pi$) without $\mathcal{T}$ symmetry. Since the change of the direction of magnetic moments will not affect the ordering of the bands at all the TRIM points, both the $afmb$ and $afmc$ phases are AI and HOTI at the same time [15], which will lead to possible chiral hinge states at the hinges between two gapped surfaces.

*Topology of the afmb phase.*—For the $afmb$ phase of $EuIn_2As_2$, the generators of the MSG include spatial inversion ($\mathcal{I}$), a twofold rotation ($C_{2y}$), and a screw rotation ($\{C_{2z}|00(c/2)\}$). Among the eight symmetry operations constructed from these generators, the following symmetries are important in the study of the $afmb$ phase: $M_y \equiv IC_{2y}$ and $M_z \equiv I\{C_{2z}|00(c/2)\}$. Beside the $\mathcal{I}$-based invariant $\mathbb{Z}_4 = 2$, we have also calculated the MCNs [40] by calculating the flow of the WANNIER charge centers on the mirror-symmetric planes in both $+i$ and $-i$ mirror eigenvalue subspaces. Our *ab initio* calculations show the $k_z = 0$ ($k_y = 0$) plane has a nontrivial mirror Chern number $n_{M_z=\pm i} = \mp 1$ ($n_{M_y=\pm i} = \mp 1$), while the $k_z = \pi$ ($k_y = \pi$) is trivial. Namely, the $afmb$ phase of $EuIn_2As_2$ is also a TCI phase with antiferromagnetic order. The nontrivial mirror Chern numbers $n_{M_z=\pm i} = \mp 1$ ($n_{M_y=\pm i} = \mp 1$)

TABLE I. The number of occupied bands of odd and even parity at the eight TRIM points, without (w/o) SOC and with (w/) SOC, respectively. The number of electrons is 146 in total.

| $\Lambda_\alpha$ | (0,0,0) | $(\pi,0,0)$ | $(0,\pi,0)$ | $(\pi,\pi,0)$ | $(0,0,\pi)$ | $(\pi,0,\pi)$ | $(0,\pi,\pi)$ | $(\pi,\pi,\pi)$ |
|---|---|---|---|---|---|---|---|---|
| Spin up w/o SOC | 41/32 | 42/31 | 42/31 | 42/31 | 40/33 | 40/33 | 40/33 | 40/33 |
| Spin down w/o SOC | 41/32 | 42/31 | 42/31 | 42/31 | 33/40 | 33/40 | 33/40 | 33/40 |
| w/SOC | 82/64 | 84/62 | 84/62 | 84/62 | 73/73 | 73/73 | 73/73 | 73/73 |

guarantee the existence of a massless Dirac cone on the $M_z$- ($M_y$-) preserving surface. The energy spectrum near the Dirac cone on (100), (010), and (001) surfaces have been calculated with the Green's function method [41,42], as shown in Figs. 3(b) and 3(d). The massless Dirac cone is constrained on the $M_y$-symmetric path $\bar{\Gamma}\bar{M}$ for the (001) surface and on the $M_z$-symmetric path $\bar{\Gamma}\bar{X}$ for the (010) surface, while for the (100) surface, the Dirac cone is localized on the $\Gamma$ point constrained by $M_y$ and $\{M_z|00(c/2)\}$ at the same time. The above numerical results confirm that, due to the coexisting nonzero mirror Chern number in the $afmb$ phase, all the low-index surfaces like (100), (010), and (001) are gapless and the chiral hinge states can be possible only on the hinges formed by two high-index surfaces which are gapped.

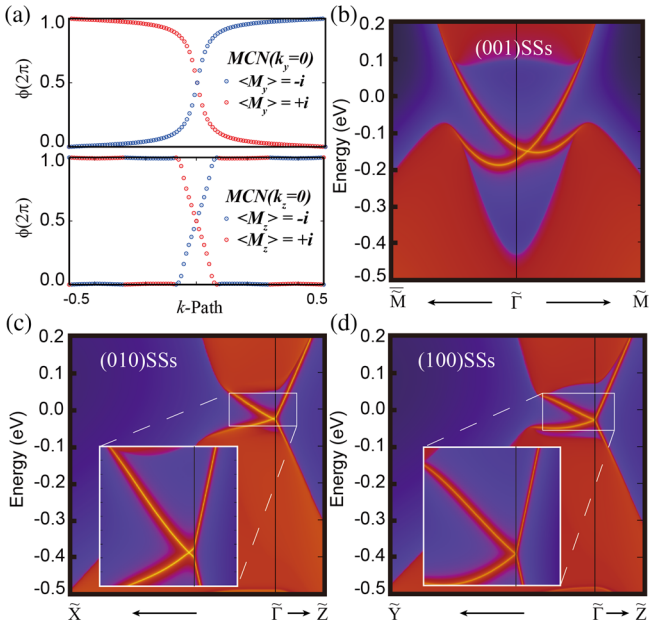


FIG. 3. Numerical calculations of the MCNs and topological surface states of the $afmb$ phase. (a) Top panel: Flow chart of the average position of WANNIER charge centers calculated by the Wilson-loop method for the occupied bands with mirror eigenvalue $\langle M_y\rangle = i\,(-i)$ on the mirror plane $k_y = 0$, which is plotted by red (blue) circles. Bottom panel: Flow chart of the average position of WANNIER charge centers calculated by the Wilson-loop method for the occupied bands with mirror eigenvalue $\langle M_z\rangle = i\,(-i)$ on the mirror plane $k_z = 0$, which is plotted by red (blue) circles. (b)–(d) are the surface states of the $afmb$ phase along the high-symmetry lines on the surface BZ of (001), (010), and (100) surface planes, respectively. (b) The Dirac cone of the (001) surface is on the path of $k_y = 0$ protected by $M_y$. (c) The Dirac cone of the (010) surface is on the path of $k_z = 0$ protected by $\{M_z|00(c/2)\}$. (d) The Dirac cone of the (100) surface is constrained on the $\Gamma$ point by $M_y$ and $\{M_z|00(c/2)\}$ symmetries.

*Higher-order topology of the afmc phase.*—When the magnetic moment is along the $c$ axis, the generators of the MSG include spatial inversion ($\mathcal{I}$), a threefold rotation ($C_{3z}$), a twofold screw rotation ($\{C_{2x}|00(c/2)\}$), and a combined antiunitary symmetry ($\mathcal{T}C_{2y}$). No symmetry-protected gapless surface state is found in our calculations for both (100) and (001) surfaces. Therefore, we can generate a hexagonal cylinder in real space (as shown in Fig. 4) with all the surfaces being gapped. But the symmetry $\mathcal{T}C_{2y}$ can relate two neighbor side surfaces and leads to mass terms with different sign on the neighboring surfaces of the hinges along the $c$ axis. Thus, 1D chiral

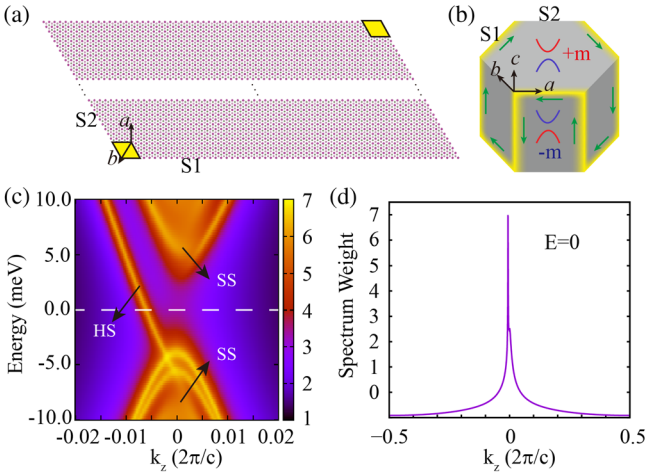


FIG. 4. Chiral hinge states (HS) of the $afmc$ phase. (a) The structural configuration used in our hinge mode calculation, which have open boundary conditions in the $S1$ and $S2$ surfaces and periodic boundary conditions in the $z$ direction. We have calculated the hinge modes with the 61-unit-cell width for the $S1$ surface and semi-infinite width for the $S2$ surface. The hinges that have chiral modes are represented by yellow regions. (b) Schematic of the 1D chiral modes that localized on the hinges of hexagonally shaped HOTI with $C_{3z}$ and $\mathcal{I}$. The regions of Dirac mass terms with opposite sign are separated by the yellow lines, which represent the chiral current channel. (c) Numerical calculations of the hinge states with the supercell structure in (a). (d) Spectrum strength on the Fermi energy along the $k_z$ direction.

models can be expected in these hinges. Based on the tight-binding Hamiltonian, we have simulated the hinge states using the Green's function method with the structural configuration in Fig. 4(a). For details of the computational method, please refer to our previous paper [15]. The energy spectrum projected onto the hinge is shown in Figs. 4(c) and 4(d), which indicates that the bulk and surface states are all gapped with a minimal gap of about 10 meV and a chiral mode exists on the hinge.

The existence of the chiral hinge states can also be derived from the following $k \cdot p$ model. The irreducible representations for the two bands near the Fermi level are $\Gamma_4^+$ and $\Gamma_4^-$ at $\Gamma$, as shown in Fig. 2(d), where $\Gamma_4^{\pm}$ are from the character table of $D_{3d}$. Based on the invariant theory, the low-energy effective Hamiltonian at the $\Gamma$ point can be described as

$$\begin{aligned} H(k) &= \epsilon(k)\mathbb{I}_{4\times 4} + M(k)\tau_z\sigma_0 + H_1 + H_2, \\ H_1 &= A(k_x\tau_x\sigma_x + k_y\tau_x\sigma_y) + Bk_z\tau_x\sigma_z, \\ H_2 &= Ck_z\tau_z(\sigma_x k_x + \sigma_y k_y) \\ &\quad + D\tau_z[\sigma_x(k_x^2 - k_y^2) - 2\sigma_y k_x k_y], \end{aligned} \tag{3}$$

where $\epsilon(k) = \epsilon_0 + \epsilon_1 k_z^2 + \epsilon_2(k_x^2 + k_y^2)$, $M(k) = M_0 + M_1 k_z^2 + M_2(k_x^2 + k_y^2)$, and $A$, $B$, $C$, and $D$ are real. $\tau$ and $\sigma$ represent the orbital and spin space, respectively. $H_{1(2)}$ is the first-(second-) order term of moment $k$. In the $afmc$ phase, $\mathcal{T}$ is broken, while the combined antiunitary symmetry of $\mathcal{T}C_{2y}$ is preserved. Under the basis, $\mathcal{T}C_{2y}$, $\mathcal{I}$, $C_{3z}$, and $\{C_{2x}|00(c/2)\}$ are represented by $\tau_z\mathcal{K}$, $\tau_z\sigma_0$, $\tau_0 e^{-i(\pi/3)\sigma_z}$, and $\tau_0 e^{-i(\pi/2)\sigma_x}$, respectively. Note that $H_1$ respects $\mathcal{T}$ symmetry ($i\sigma_y\mathcal{K}$), but $H_2$ breaks it. Thus, the term $f(k)\tau_y\sigma_0$ can be added to the $k \cdot p$ Hamiltonian of the sample, which is invariant, $R[f(k)\tau_y\sigma_0]R^{-1} = f(Rk)\tau_y\sigma_0$, under the symmetries ($R = \mathcal{T}C_{2y}$, $C_{2x}$, $\mathcal{I}$, and $C_{3z}$):

$$\begin{aligned} f(\mathcal{T}C_{2y}k) &= f(k); \qquad f(C_{2x}k) = f(k); \\ f(\mathcal{I}k) &= -f(k); \qquad f(C_{3z}k) = f(k). \end{aligned} \tag{4}$$

Thus, to the lowest order of $k$, $f(k) = F(k_x^3 - 3k_x k_y^2)$. By projecting the bulk Hamiltonian onto the surface [43], the resulting mass term changes its sign under $\mathcal{I}$ symmetry and invariant under threefold rotation symmetry $C_{3z}$. So for the shaped crystal structure shown in Fig. 4(b), there will be chiral modes, indicated by the green arrows. Therefore, the HOTI phase in the present system is similar to the case in bismuth, but it is chiral instead of helical in the case of bismuth.

*Conclusion.*—In summary, we propose that the 3D antiferromagnetic material $EuIn_2As_2$ is an axion insulator with a quantized TME effect in the bulk. Its nontrivial topology can be characterized by the parity-based invariant $\mathbb{Z}_4 = 2$. With the AFM moments pointing along $a$ or $b$ axis, it is also a TCI with *nonzero* mirror Chern numbers. Its gapless surface states have been calculated on both side and top surfaces, protected by mirror symmetries. When the easy AFM moments are pointing along the $c$ axis, the (100) and (001) surfaces are gapped and it is also a HOTI with all the side surfaces fully gapped. We have also calculated the chiral hinge modes in this material system, which exist on the sample of a hexagonal rod. The HOTI phase and its chiral hinge modes in the present system are protected by inversion symmetry with $\mathbb{Z}_4 = 2$. As $EuIn_2As_2$ is easy to grow and the magnetic configuration is intrinsic, it is an ideal candidate to study axion insulators and HOTIs. It also provides a platform to study the interplay between the magnetic structure and the topological features of the band structure.

We thank Jinjian Zhou for helpful discussions on the nodal lines without SOC. Z. W. was supported by the National Thousand-Young-Talents Program, the CAS Pioneer Hundred Talents Program, and the National Natural Science Foundation of China. H. W. acknowledges support from the Ministry of Science and Technology of China under Grants No. 2016YFA0300600 and No. 2018YFA0305700, the Chinese Academy of Sciences under Grant No. XDB28000000, the Science Challenge Project (No. TZ2016004), the K. C. Wong Education Foundation (GJTD-2018-01), Beijing Municipal Science and Technology Commission (Z181100004218001), and Beijing Natural Science Foundation (Z180008). X. D. acknowledges financial support from the Hong Kong Research Grants Council (Project No. GRF16300918).

*Note added.*—We are also aware of the similar work [37] when finalizing the present Letter.

*hmweng@iphy.ac.cn
†daix@ust.hk

[1] R. D. Peccei and H. R. Quinn, Phys. Rev. Lett. **38**, 1440 (1977).
[2] F. Wilczek, Phys. Rev. Lett. **58**, 1799 (1987).
[3] X.-L. Qi, T. L. Hughes, and S.-C. Zhang, Phys. Rev. B **78**, 195424 (2008).
[4] A. M. Turner, Y. Zhang, R. S. K. Mong, and A. Vishwanath, Phys. Rev. B **85**, 165120 (2012).
[5] H. Watanabe, H. C. Po, and A. Vishwanath, Sci. Adv. **4**, eaat8685 (2018).
[6] S. Ono and H. Watanabe, Phys. Rev. B **98**, 115150 (2018).
[7] A. M. Essin, J. E. Moore, and D. Vanderbilt, Phys. Rev. Lett. **102**, 146805 (2009).
[8] W. A. Benalcazar, B. A. Bernevig, and T. L. Hughes, Phys. Rev. B **96**, 245115 (2017).
[9] J. Langbehn, Y. Peng, L. Trifunovic, F. von Oppen, and P. W. Brouwer, Phys. Rev. Lett. **119**, 246401 (2017).
[10] W. A. Benalcazar, B. A. Bernevig, and T. L. Hughes, Science **357**, 61 (2017).

[11] Z. Song, Z. Fang, and C. Fang, Phys. Rev. Lett. **119**, 246402 (2017).
[12] F. Schindler, A. M. Cook, M. G. Vergniory, Z. Wang, S. S. Parkin, B. A. Bernevig, and T. Neupert, Sci. Adv. **4**, eaat0346 (2018).
[13] F. Schindler, Z. Wang, M. G. Vergniory, A. M. Cook, A. Murani, S. Sengupta, A. Y. Kasumov, R. Deblock, S. Jeon, I. Drozdov *et al.*, Nat. Phys. **14**, 918 (2018).
[14] M. Ezawa, Phys. Rev. B **97**, 155305 (2018).
[15] C. Yue, Y. Xu, Z. Song, H. Weng, Y.-M. Lu, C. Fang, and X. Dai, Nat. Phys. **15**, 577 (2019).
[16] N. Okuma, M. Sato, and K. Shiozaki, Phys. Rev. B **99**, 085127 (2019).
[17] Z. Wang, B. J. Wieder, J. Li, B. Yan, and B. A. Bernevig, arXiv:1806.11116.
[18] B. J. Wieder and B. A. Bernevig, arXiv:1810.02373.
[19] D. Xiao, J. Jiang, J.-H. Shin, W. Wang, F. Wang, Y.-F. Zhao, C. Liu, W. Wu, M. H. W. Chan, N. Samarth, and C.-Z. Chang, Phys. Rev. Lett. **120**, 056801 (2018).
[20] M. Mogi, M. Kawamura, R. Yoshimi, A. Tsukazaki, Y. Kozuka, N. Shirakawa, K. Takahashi, M. Kawasaki, and Y. Tokura, Nat. Mater. **16**, 516 (2017).
[21] R. Li, J. Wang, X.-L. Qi, and S.-C. Zhang, Nat. Phys. **6**, 284 (2010).
[22] X. Wan, A. Vishwanath, and S. Y. Savrasov, Phys. Rev. Lett. **108**, 146601 (2012).
[23] D. Zhang, M. Shi, K. He, D. Xing, H. Zhang, and J. Wang, Phys. Rev. Lett. **122**, 206401 (2019).
[24] J. Li, Y. Li, S. Du, Z. Wang, B.-L. Gu, S.-C. Zhang, K. He, W. Duan, and Y. Xu, arXiv:1808.08608.
[25] Y. Gong, J. Guo, J. Li, K. Zhu, M. Liao, X. Liu, Q. Zhang, L. Gu, L. Tang, X. Feng *et al.*, arXiv:1809.07926.
[26] S. Chowdhury, K. F. Garrity, and F. Tavazza, npj Comput. Mater. **5**, 33 (2019).
[27] A. M. Goforth, P. Klavins, J. C. Fettinger, and S. M. Kauzlarich, Inorg. Chem. **47**, 11048 (2008).
[28] N. Singh and U. Schwingenschlögl, Appl. Phys. Lett. **100**, 151906 (2012).
[29] G. Kresse and J. Furthmüller, Phys. Rev. B **54**, 11169 (1996).
[30] G. Kresse and J. Hafner, Phys. Rev. B **47**, 558 (1993).
[31] J. P. Perdew, K. Burke, and M. Ernzerhof, Phys. Rev. Lett. **77**, 3865 (1996).
[32] P. E. Blöchl, Phys. Rev. B **50**, 17953 (1994).
[33] J. P. Perdew, K. Burke, and M. Ernzerhof, Phys. Rev. Lett. **77**, 3865 (1996).
[34] S. L. Dudarev, G. A. Botton, S. Y. Savrasov, C. J. Humphreys, and A. P. Sutton, Phys. Rev. B **57**, 1505 (1998).
[35] I. Souza, N. Marzari, and D. Vanderbilt, Phys. Rev. B **65**, 035109 (2001).
[36] P. Richard, C. Capan, J. Ma, P. Zhang, N. Xu, T. Qian, J. Denlinger, G. Chen, A. Sefat, Z. Fisk *et al.*, J. Phys. Condens. Matter **26**, 035702 (2014).
[37] X. Gui, I. Pletikosic, H. Cao, H.-J. Tien, X. Xu, R. Zhong, G. Wang, T.-R. Chang, S. Jia, T. Valla *et al.*, arXiv:1903.03888.
[38] F. Tran and P. Blaha, Phys. Rev. Lett. **102**, 226401 (2009).
[39] See Supplemental Material at http://link.aps.org/supplemental/10.1103/PhysRevLett.122.256402 for band structure near Γ point calculated with modified Becke-Johnson potential.
[40] T. H. Hsieh, H. Lin, J. Liu, W. Duan, A. Bansil, and L. Fu, Nat. Commun. **3**, 982 (2012).
[41] M. L. Sancho, J. L. Sancho, J. L. Sancho, and J. Rubio, J. Phys. F **15**, 851 (1985).
[42] Q. Wu, S. Zhang, H.-F. Song, M. Troyer, and A. A. Soluyanov, Comput. Phys. Commun. **224**, 405 (2018).
[43] E. Khalaf, H. C. Po, A. Vishwanath, and H. Watanabe, Phys. Rev. X **8**, 031070 (2018).